Identification of Axon Bendings in Neurons by Multiphysics FEM Simulations of High-Density MEA Extracellular Recordings

Federico Leva[1*], Andrea Corna[2], Paul Werginz[2], Pierpaolo Palestri[3], Günter Zeck[2], Luca Selmi[1]
[1]*Department of Engineering "Enzo Ferrari", Università degli studi di Modena e Reggio Emilia , Modena, Italy*
[2]*Institute of Biomedical Electronics, Technische Universität Wien, Vienna, Austria.*
[3]*DPIA, Polytechnic Department of Engineering and Architecture, University of Udine, Udine, Italy*
[*]E-mail: federico.leva@unimore.it

***Abstract*—A three-dimensional finite element method (FEM) simulation of a neuron (retinal ganglion cell) interfaced to a high-density CMOS-based microelectrode array (MEA) is performed and compared to recordings. The adopted multiscale simulation approach accurately reproduces the signals recorded by the patch clamp and the MEA sensors. The simulation leads us to identify bendings of the axon initial segment of a few neurons embedded in tissue, which are reported here for the first time.**

***Index Terms*—Retinal ganglion cell, CMOS-MEA, Neural recording, FEM simulations, Extracellular signal sensing**

I. Introduction

Patch clamps and microelectrode arrays (MEAs) are the gold standard technologies for intracellular neuronal electrophysiology and extracellular electrical imaging and recording, respectively [1]–[3]. While the former method is limited to simultaneously record from one to ten cells or even from fewer positions on a single cell at a time, the latter allows for simultaneous electrical imaging from a large population [4] but usually with one recording site/cell. However, intracellular probes affect and damage neurons, hampering the stability and repeatability of the experiments. On the contrary, extracellular recordings provide better long-term stability, but also lower amplitude signals of uncertain interpretation due to the imperfect coupling and partly unknown transduction between the sensor and the neuron. None of the techniques provides a detailed map of the initiation of an action potential and its propagation within and along cellular compartments.

Physics-based full three-dimensional (3D) finite-element method (FEM) simulations [5]–[7] can provide insights and support the interpretation of intra- and extracellular recordings. However, in most instances, only one electrode is considered, and the electrolyte is assumed purely ohmic [8]–[10].

In this paper we develop a full 3D FEM model coupling a distributed Hodgkin-Huxley description of the generative functions of retinal ganglion cells (RGCs) with a microscopic representation of the intra- and extracellular electrolytes via a Poisson-Nernst-Planck model, and with a detailed representation of the sensing electrodes pattern.

The complete 3D model accurately reproduces the MEA recordings of RGCs in tissue with subcompartmental resolution. We found that a few neurons exhibit U- and L-shaped bendings of the axon initial segments, a feature that can be non-ambiguously assessed only by combining MEA recordings and advanced optical imaging [11], [12].

This work has been partially supported by the European Union's Horizon-2020 project "IN-FET" (GA n. 862882) via the IUNET consortium, and by the Austrian Science Fund (FWF, 35488).

II. Methods

Extracellular recording from ex-vivo retinal ganglion cell. A CMOS-MEA comprising $65\times65 = 4225$ sensor sites at a 16 μm pitch was used to record extracellular voltages [13] from neurons in the ex-vivo retina of adult (>90 days) B6.CXB1-Pde6brd10/J (retinal degeneration 10 (rd10)) mice. The retina was isolated from the enucleated eye and a portion was interfaced in epiretinal configuration with the sensor sites previously coated with poly-L-lysine (P1399, MW 150–300 kDa, Sigma, Germany). Retina samples were dark adapted for 30-45 minutes before recording and kept in heated (32-35° C) and carbogenated (95%O2, 5%CO2) Ames' medium (Ames A 1420, Sigma Aldrich + NaHCO3) during the recording. The experimental procedures to prepare the ex vivo retina were reported and approved by the Center for Biomedical Research, Medical University Vienna, Austria. Extracellular voltages (V_{se} in the following) were recorded at 20 kHz and high-pass filtered at 10 Hz. A Spike Triggered Average (STA) was performed after spike sorting [14] to reduce the noise on the raw traces and obtain electrical images of one single ganglion cell neuron in terms of spatiotemporal maps.

Multiphysics FEM simulation setup. The new simulation framework significantly extends our previous work (limited to a single electrode and simplified neuron geometry with cylindrical symmetry) [15] by considering the full 3D geometry of an RGC coupled with the CMOS-MEA. The descriptions of the intra- and extracellular electrolyte models, the ion transport across the neuron membrane, the Hodgkin-Huxley-like action potential dynamics, and the sensing electrode are mostly as in [15]. Notable additions are the implementation of a compartmentalized 3D RGC morphology and physiology coupled to multiple electrodes in the CMOS-MEA, as discussed below.

Figure 1 shows the morphology and dimensions of the simulated RGC [16], [17], of the tissue [18], and of the MEA [13]. Similarly to [7], we: i) represent the soma as a sphere, ii) simplify complex dendritic tree ramifications with two dendrite segments; iii) replicate the axonal branch with a series of straight segments with tapered diameter [17], aligned in the

same direction to reduce the total domain dimensions and save mesh points. Nevertheless, the FEM description of the neuron retains the presence of dendrites, soma, hillock, and initial and distal axon compartments with the same surface area as those traced from real samples [16]. The neuron biophysical properties (i.e., parameters of the ion channels, intracellular resistivity, etc.) are also taken from [16], with minor adjustments of a specific set of ion conductances in each compartment, as summarized in Table I. This approach is consistent with other FEM implementations [5]–[7] which, however, assume ohmic cellular fluids.

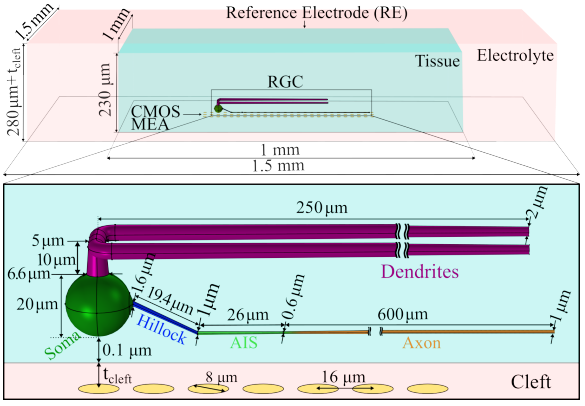

Fig. 1: Multiscale 3D representation of the FEM simulation setup consisting of extracellular electrolyte, tissue, RGC, and a few sensor sites of the CMOS-MEA domains. The inset zooms on the RGC, and differentiates its morphological compartments by color. Notice the tapering of the hillock, AIS, and axon diameters as in [17]. At the bottom, seven sensor sites of the CMOS-MEA are shown, out of 120 simulated.

The dynamical model of the action potentials (APs) for each compartment is set by the Hodgkin-Huxley membrane equations vs time (t) as follows:

$$C_{\mathrm{m}}\frac{dV}{dt} = I_{\mathrm{K}}(V,n,\overline{g}_{\mathrm{K}}) + I_{\mathrm{Na}}(V,m,h,\overline{g}_{\mathrm{Na}}) + I_{\mathrm{L}}(V,\overline{g}_{\mathrm{L}}) + I_{\mathrm{Ca}}(V,c,\overline{g}_{\mathrm{Ca}}) + I_{\mathrm{KCa}}(V,\left[\mathrm{Ca}^{2+}\right],\overline{g}_{\mathrm{KCa}}) + I_{\mathrm{Stim}} \quad (1)$$

$$\frac{dq}{dt} = Q10\left(\alpha_q(V)(1-q) - \beta_q(V)q\right) \text{ for } q = n,m,h,c \quad (2)$$

where C_{m} is the membrane capacitance per unit area, V is the membrane potential, I_{K}, I_{Na}, I_{Ca}, I_{KCa}, I_{L} are respectively the Potassium, Sodium, Calcium, Calcium-driven Potassium, individual Leakage ion current fluxes, n, m, h, c, are the instantaneous gating variables, $\left[\mathrm{Ca}^{2+}\right]$ is the instantaneous intracellular Calcium concentration, $Q10$ is the kinetic prefactor multiplying all $\alpha_q(V)$ and $\beta_q(V)$ gating functions [16], [19], $\overline{g}_{\mathrm{K}}$, $\overline{g}_{\mathrm{Na}}$, $\overline{g}_{\mathrm{Ca}}$, $\overline{g}_{\mathrm{KCa}}$, $\overline{g}_{\mathrm{L}}$ are given in Table I.

I_{Stim} is a distributed stimulation current, implemented as a Sodium transmembrane current (with a step function in time), mimicking the synaptic current mediated by excitatory presynaptic neurons [20]. To emulate patch clamp experiments, we apply a very small I_{Stim} across the soma [21]. When simulating the extracellular recording of spontaneous APs, we distribute a small I_{Stim} across the dendrites' surface. The small current induces only a modest stimulation artifact on the recorded signals (see Figure 3 and Figure 4 in section III).

TABLE I: Model parameters used in this work.

Symbol	Value/expression				Units	Ref.
	Bulk	Tissue	Cleft	Cytosol		
ε_r	80	80	80	80	1	
ρ	66	5000	100	143	Ω·cm	
$[\mathrm{K}^+]_0$	4	4	4	140	mM	[23]
$[\mathrm{Na}^+]_0$	144	144	144	18	mM	[23]
$[\mathrm{Cl}^-]_0$	130	130	130	6	mM	[24]
$[\mathrm{Ca}^{2+}]_0$	1.8	1.8	1.8	10^{-4}	mM	[16]
[a] $[\mathrm{A}^-]_0$	21.6	21.6	21.6	152	mM	
[b] $\mathrm{D}_{\mathrm{K}+}$	17.54	0.23	11.57	12.15	$10^{-10}\mathrm{m}^2/\mathrm{s}$	[25]
[b] $\mathrm{D}_{\mathrm{Na}+}$	11.90	0.16	7.85	8.24	$10^{-10}\mathrm{m}^2/\mathrm{s}$	[25]
[b] $\mathrm{D}_{\mathrm{Cl}-}$	18.16	0.24	11.99	12.58	$10^{-10}\mathrm{m}^2/\mathrm{s}$	[25]
[b] $\mathrm{D}_{\mathrm{Ca2+}}$	7.09	0.09	4.68	4.92	$10^{-10}\mathrm{m}^2/\mathrm{s}$	[25]
[a] $\mathrm{D}_{\mathrm{A}-}$	1	1	1	1	$10^{-25}\mathrm{m}^2/\mathrm{s}$	
	Dendrite	Soma	Hillock	AIS	Axon		
$\overline{g}_{\mathrm{Na}}$	79.5·γ_{Na}	72.0	141.1	231.1	124.0.0	mS/cm^2	[16]
$\overline{g}_{\mathrm{K}}$	23.4·γ_{K}	50.4	67.8	74.6	50.0	mS/cm^2	[16]
$\overline{g}_{\mathrm{Ca}}$	1.2	1.2	0.753	0.0	0.0	mS/cm^2	[16]
$\overline{g}_{\mathrm{KCa}}$	0.15	0.15	0.15	0.15	0.15	mS/cm^2	[16]
$\overline{g}_{\mathrm{L}}$	0.1	0.1	0.1	0.1	0.1	mS/cm^2	[16]

ε_r medium relative permittivity, ρ medium resistivity, $[\mathrm{X}_i]_0$ baseline concentration of the i-th ion, D_{X_i} diffusion coefficient of the i-th ion, $\overline{g}_{\mathrm{X}_i}$ maximum channel conductance for the i-th ion, γ_{Na} and γ_{K} adjustment factors. [a]Set to provide baseline electroneutrality. [b]Set to yield the exact resistivity value of the ρ above.

Last but not least, we examined the active CMOS readout underneath each microelectrode. Since the sensing electrode coupling capacitance (1 pF) is much larger than the parallel of the gate-oxide capacitance of the sensing MOSFET (130 fF) and the parasitic capacitance (12.3 fF) [22], the transduction gain is essentially one, and the recorded signal is approximately equal to the potential difference between the sensing electrode surface, V_{se}, and the reference electrode.

The large simulation domain is densely meshed for the neuron and the electrode; a coarse mesh is used for the remaining parts. The *swept mesh* option of [26] is extensively used for the tissue and cleft regions below the neuron where finely meshed electrical double layers decay without overburdens in the in-plane directions. A *swept mesh* is used also for the dendrites (with a coarse free triangular cross-section) and for the long axon (with a fine boundary layer cross-section). The final mesh has 652389 elements and yields 1907731 *degrees of freedom (DOF)* [26]. Transient simulations run in ≈10000 seconds on a 104-core Intel Xeon Gold server with 512 GB RAM.

III. Results and Conclusions

This section compares the simulated and experimental intra- and extracellular action potentials as a means to validate the accuracy of the 3D FEM RGC model surrounded by tissue and electrolyte, in the proximity of the MEA. To quantify the agreement between the simulated, $s(t)$, and experimental traces, $e(t)$, we use the cosine similarity factor S:

$$S = \frac{\int_t s(t)\cdot e(t)\,dt}{\sqrt{\int_t s^2(t)\,dt}\cdot\sqrt{\int_t e^2(t)\,dt}}. \quad (3)$$

Figure 2 shows that the simulated membrane somatic potential matches with a very high similarity factor (S=0.999) the experimental patch clamp recording from [21]. The free model parameters ($Q10$, γ_{K}, γ_{Na}) have been adjusted as reported in

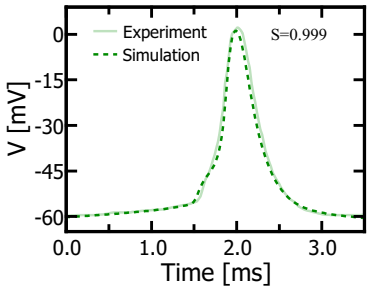

Fig. 2: Simulated somatic action potential vs experimental patch clamp recording from [21]. Parameters: $Q10 = 0.7155$, $\gamma_{\mathrm{Na}} = 0.4$ $\gamma_{\mathrm{K}} = 0.6$, $I_{\mathrm{Stim}} = 150$ pA applied to the soma. The line color matches the soma compartment color in Fig. 1.

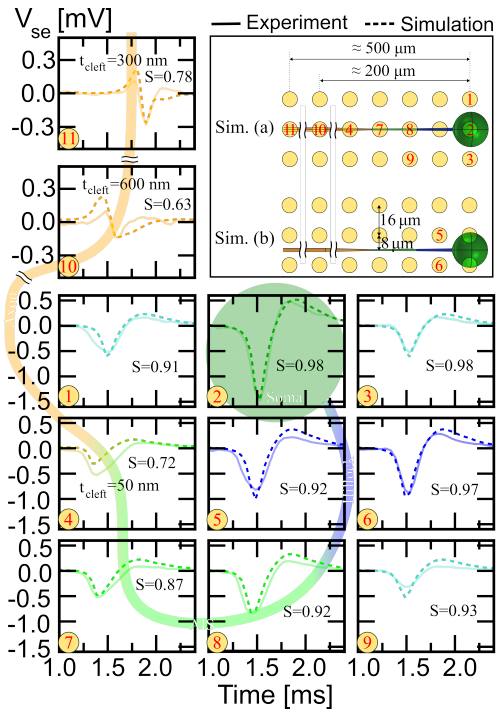

Fig. 3: Simulated extracellular action potentials vs experimental MEA recordings. Parameters: $Q10 = 0.28$, $\gamma_{\mathrm{Na}} = 0.52$, $\gamma_{\mathrm{K}} = 1.65$, $I_{\mathrm{Stim}} = 320$ pA applied to the dendrites, $t_{\mathrm{cleft}} = 100$ nm if not otherwise stated. The line color matches either the overlaid neuron compartment or the tissue color in Fig. 1.

the caption. The result proves that the model can accurately reproduce the dynamics of the RGC under study.

Figure 3 and Figure 4 compare simulated and experimental extracellular signals for two different cells. To this end, firstly the in-plane and vertical position of the RGC's soma w.r.t. the nearest electrodes has been optimized in simulation to best match the measured signals (see electrode maps in the top right corners). Then, by careful scrutiny of the signals' shape, amplitude, and timing, the most likely position, height, and distance from the soma of the RGC were found for all other electrodes (see numbering in red). This allows us to identify which subcompartment has generated each signal

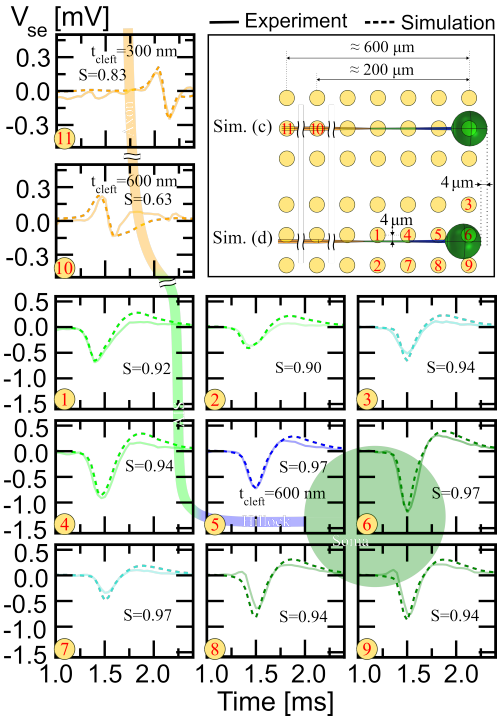

Fig. 4: Same as in Figure 3 but for a different cell and for $t_{\mathrm{cleft}} = 200$ nm if not otherwise stated.

and label it onto the corresponding experimental recording electrode. In this way subcompartmental electrical imaging is achieved (i.e., a mapping of the signals to the originating neuron subcompartment), a feature that clearly extends beyond classical spike sorting.

The simulation-aided subcompartmental mapping predicts a U-shaped bending of the AIS in the perisomatic region for the cell in Figure 3, and an L-shaped bending of the AIS for the cell in Figure 4 consistent with previous observations using optical fluorescent dyes [17]. In both cases, the S factor is usually close to 1, except for: i) axonal signals, likely because their low-amplitude signals, differently from the large-amplitude perisomatic ones, have been extracted from noise by STA and/or because the axon detaches from the MEA surface (i.e., large t_{cleft}); ii) the distal AIS in panel 4 of Figure 3, possibly because in the experiments the large signal of the U-shaped AIS sensed by the electrode is disturbed by the large perisomatic signal of the neighboring subcompartments, whereas simulations refer to a straight axon.

In Conclusion, we investigated by experiments and 3D multiphysics simulations patch clamp and CMOS-MEAs extracellular recordings of RGC. The model supports subcompartmental mapping of the signals and tracing of the RGCs spatial distribution across electrodes, thus providing valuable insights into neuron morphology and activity. The combined use of extensive physics-based FEM simulations and MEA measurements foster the identification of those highly sensitive neuron regions where high-resolution, subcompartmental, selective stimulation might be possible.

REFERENCES

[1] M. E. Spira and A. Hai, "Multi-electrode array technologies for neuroscience and cardiology," *Nature nanotechnology*, vol. 8, no. 2, pp. 83–94, 2013. 10.1038/nnano.2012.265.

[2] A. Tanwar, H. A. Gandhi, D. Kushwaha, and J. Bhattacharya, "A review on microelectrode array fabrication techniques and their applications," *Materials Today Chemistry*, vol. 26, 12 2022. 10.1016/j.mtchem.2022.101153.

[3] G. Zeck, F. Jetter, L. Channappa, G. Bertotti, and R. Thewes, "Electrical Imaging: Investigating Cellular Function at High Resolution," 11 2017. 10.1002/adbi.201700107.

[4] D. Tsai, D. Sawyer, A. Bradd, R. Yuste, and K. L. Shepard, "A very large-scale microelectrode array for cellular-resolution electrophysiology," *Nature Communications*, vol. 8, 12 2017. 10.1038/s41467-017-02009-x.

[5] C. Moulin, A. Glière, D. Barbier, S. Joucla, B. Yvert, P. Mailley, and R. Guillemaud, "A new 3-D finite-element model based on thin-film approximation for microelectrode array recording of extracellular action potential," *IEEE Transactions on Biomedical Engineering*, vol. 55, no. 2, 2008. 10.1109/TBME.2007.903522.

[6] R. Bestel, U. Van Rienen, C. Thielemann, and R. Appali, "Influence of Neuronal Morphology on the Shape of Extracellular Recordings with Microelectrode Arrays: A Finite Element Analysis," *IEEE Transactions on Biomedical Engineering*, vol. 68, no. 4, 2021. 10.1109/TBME.2020.3026635.

[7] A. Fellner, A. Heshmat, P. Werginz, and F. Rattay, "A finite element method framework to model extracellular neural stimulation," *Journal of Neural Engineering*, vol. 19, p. 022001, apr 2022. 10.1088/1741-2552/ac6060.

[8] R. Schätzthauer and P. Fromherz, "Neuron–silicon junction with voltage-gated ionic currents," *European Journal of Neuroscience*, vol. 10, no. 6, pp. 1956–1962, 1998. 10.1046/j.1460-9568.1998.00205.x.

[9] P. Massobrio, G. Massobrio, and S. Martinoia, "Interfacing cultured neurons to microtransducers arrays: A review of the neuro-electronic junction models," *Frontiers in Neuroscience*, vol. 10, no. JUN, 2016. 10.3389/fnins.2016.00282.

[10] G. Massobrio, S. Martinoia, and P. Massobrio, "Equivalent circuit of the neuro-electronic junction for signal recordings from planar and engulfed micro-nano-electrodes," *IEEE Transactions on Biomedical Circuits and Systems*, vol. 12, no. 1, pp. 3–12, 2018. 10.1109/TBCAS.2017.2749451.

[11] D. J. Bakkum, U. Frey, M. Radivojevic, T. L. Russell, J. Müller, M. Fiscella, H. Takahashi, and A. Hierlemann, "Tracking axonal action potential propagation on a high-density microelectrode array across hundreds of sites," *Nature communications*, vol. 4, no. 1, p. 2181, 2013. 10.1038/ncomms3181.

[12] M. Radivojevic, D. Jäckel, M. Altermatt, J. Müller, V. Viswam, A. Hierlemann, and D. J. Bakkum, "Electrical identification and selective microstimulation of neuronal compartments based on features of extracellular action potentials," *Scientific reports*, vol. 6, no. 1, pp. 1–20, 2016. 10.1038/srep31332.

[13] Multi Channel Systems website: https://www.multichannelsystems.com.

[14] C. Leibig, T. Wachtler, and G. Zeck, "Unsupervised neural spike sorting for high-density microelectrode arrays with convolutive independent component analysis," *Journal of Neuroscience Methods*, vol. 271, pp. 1–13, 2016. 10.1016/j.jneumeth.2016.06.006.

[15] F. Leva, C. Verardo, P. Palestri, and L. Selmi, "Multiphysics finite-element modeling of the neuron/electrode electrodiffusive interaction," in *2022 IEEE Sensors*, IEEE, 2022. 10.1109/SENSORS52175.2022.9967049.

[16] J. F. Fohlmeister, E. D. Cohen, and E. A. Newman, "Mechanisms and distribution of ion channels in retinal ganglion cells: Using temperature as an independent variable," *Journal of Neurophysiology*, vol. 103, no. 3, pp. 1357–1374, 2010. PMID: 20053849.

[17] V. Raghuram, P. Werginz, and S. I. Fried, "Scaling of the ais and somatodendritic compartments in α s rgcs," *Frontiers in Cellular Neuroscience*, vol. 13, 2019. 10.1152/jn.00123.2009.

[18] L. R. Ferguson, J. M. Dominguez II, S. Balaiya, S. Grover, and K. V. Chalam, "Retinal thickness normative data in wild-type mice using customized miniature sd-oct," *PloS one*, vol. 8, no. 6, p. e67265, 2013. 10.1371/journal.pone.0067265.

[19] J. Fohlmeister, P. Coleman, and R. F. Miller, "Modeling the repetitive firing of retinal ganglion cells," *Brain research*, vol. 510, no. 2, pp. 343–345, 1990. 10.1016/0006-8993(90)91388-W.

[20] R. Jolivet, J. S. Coggan, I. Allaman, and P. J. Magistretti, "Multi-timescale Modeling of Activity-Dependent Metabolic Coupling in the Neuron-Glia-Vasculature Ensemble," *PLoS Computational Biology*, vol. 11, no. 2, 2015. 10.1371/journal.pcbi.1004036.

[21] P. Werginz, V. Raghuram, and S. I. Fried, "Tailoring of the axon initial segment shapes the conversion of synaptic inputs into spiking output in off-α; t retinal ganglion cells," *Science Advances*, vol. 6, no. 37, p. eabb6642, 2020. 10.1126/sciadv.abb6642.

[22] G. Bertotti, F. Jetter, N. Dodel, S. Keil, C. Boucsein, A. Möller, K.-H. Boven, G. Zeck, and R. Thewes, "Artifact-compensated time-continuous recording from neural tissue during stimulation using a capacitively coupled in-vitro cmos-mea with 4k recording and 1k stimulation sites," in *2016 IEEE Biomedical Circuits and Systems Conference (BioCAS)*, pp. 256–259, IEEE, 2016. 10.1109/BioCAS.2016.7833780.

[23] W. Gerstner, M. W. Kistler, R. Naud, and L. Paninski, *Neuronal Dynamics - From single neurons to networks and models of cognition*. Cambridge University Press, 1sr ed. ed., 2014.

[24] J. R. Cressman, G. Ullah, J. Ziburkus, S. J. Schiff, and E. Barreto, "The influence of sodium and potassium dynamics on excitability, seizures, and the stability of persistent states: I. Single neuron dynamics," *Journal of Computational Neuroscience*, vol. 26, no. 2, pp. 159–170, 2009. 10.1007/s10827-008-0132-4.

[25] L. Yuan-Hui and S. Gregory, "Diffusion of ions in sea water and in deep-sea sediments," *Geochimica et cosmochimica acta*, vol. 38, no. 5, pp. 703–714, 1974. 10.1016/0016-7037(74)90145-8.

[26] Comsol, Inc., Comsol Multiphysics v. 6.0.